

## EVALUATION OF SOLIDIFICATION IN POWDER BED FUSION USING A HIGH SPEED CAMERA

H. Merschroth\*, J. Harbig\*, M. Weigold\*, J. Geis†, and E. Kirchner†

\*Institute of Production Management, Technology and Machine Tools, TU Darmstadt, Germany

†Product Development and Machine Elements, TU Darmstadt, Germany

### Abstract

Powder bed fusion using a laser beam (PBF-LB) [1] enables geometrical design freedom to build parts for optimized functionality. Furthermore, PBF-LB allows microstructural design freedom. By controlling the solidification behavior microstructural adaptions can be made to obtain the full potential of the material. As the solidification rates and the thermal gradient depend on the local part geometry, new data-driven approaches, e.g. machine learning (ML), seem to be suitable for local microstructural adaptions. In this work an evaluation concept to analyze the thermal melt pool characteristics based on a high-speed camera is developed. The thermal radiation intensity of the melt pool is used to derive the thermal gradient and combined with an image rate of 41,000 fps the solidification rate is derived. The developed approach provides local data of the solidification for ML-based process adaptions but also serves for part individual quality assurance tasks.

### Introduction

Additive Manufacturing (AM) has shown its potential of flexible manufacturing to replace cut off value chains during covid-pandemic since 2020 [2]. In addition, AM enables socially requested resource-efficient manufacturing of critical alloys, e.g. rare-earth-alloys [3]. During the past years metal-based AM has been established widely. When it comes to high quality with good reproducibility, PBF-LB is used [4]. Based on a layer by layer applied powder bed, the part geometry is exposed using a laser beam to fuse the metal powder to a dense part. This melting process determines the resulting part properties and is therefore object of current research [5,6]. The layer-by-layer build up enables the use of process monitoring systems to observe and evaluate the process over the complete part. Furthermore, data driven approaches can be derived to control the process to achieve graded microstructure and therefore improved part functionality [6].

Part properties can be estimated by its microstructure and geometry, including microstructural defects such as pores, cracks and chemical separation. Most scientific works focus on process anomaly detection and therefore estimate defects whereas the evaluation of microstructural properties such as grain size is often neglected [7].

The microstructural crystal growth depends on local cooling rate, solidification speed and nucleation [8]. The grow direction can be estimated by the temperature gradient (Figure 1). Concurring grain growth with misorientation leads to grain boundaries, which can be divided into low angle grain boundary (LAGB) and high angle grain boundary (HAGB) [9]. HAGBs have significant higher interfacial energy, which serves as resistor to dislocations and therefore increases

mechanical strength. Smaller grains lead to subsequently to more interfaces and therefore higher overall interfacial energy leading to higher mechanical strength [9].

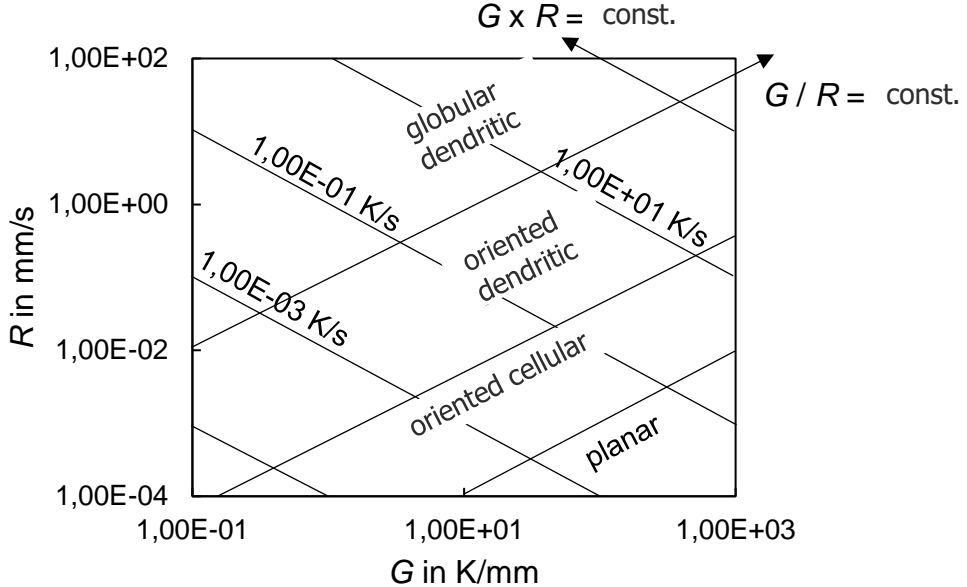


Figure 1: Graphical illustration of the correlation between solidification rate  $R$ , thermal gradient  $G$  and the resulting microstructure (based on [10])

The solidification rate  $R$  and the temperature gradient  $G$  depend on the part geometry, material and process parameters (Figure 1). High volume energy input of  $200 \text{ J/mm}^3$  leads to bigger melt pools and therefore homogenous temperature gradients. This results in grains with an average length of  $200 \mu\text{m}$ . Low energy input of  $58 \text{ J/mm}^3$  leads to smaller grains with a length up to  $100 \mu\text{m}$ . [11]

To observe the process, multiple approaches have been developed [12,13]. Pyrometers (Melt Pool Monitoring, MPM) up to  $100 \text{ kHz}$  [14] are used to evaluate the process dynamics whereas thermographic cameras with up to  $50 \text{ kHz}$  [15] are used to evaluate the temperature. When it comes to multiphase-state where solid, liquid and vapor co-exist, an evaluation using a thermographic camera is difficult as it is only calibrated to a specified phase and temperature range [16]. Pyrometers are used to measure one value each time step, which does not represent the geometric thermal distribution of the melt pool. An evaluation of temperature gradients and cooling rates is therefore not possible. However, the recorded information are used to understand the process, e.g. melting behavior, and furthermore to adopt the process [17].

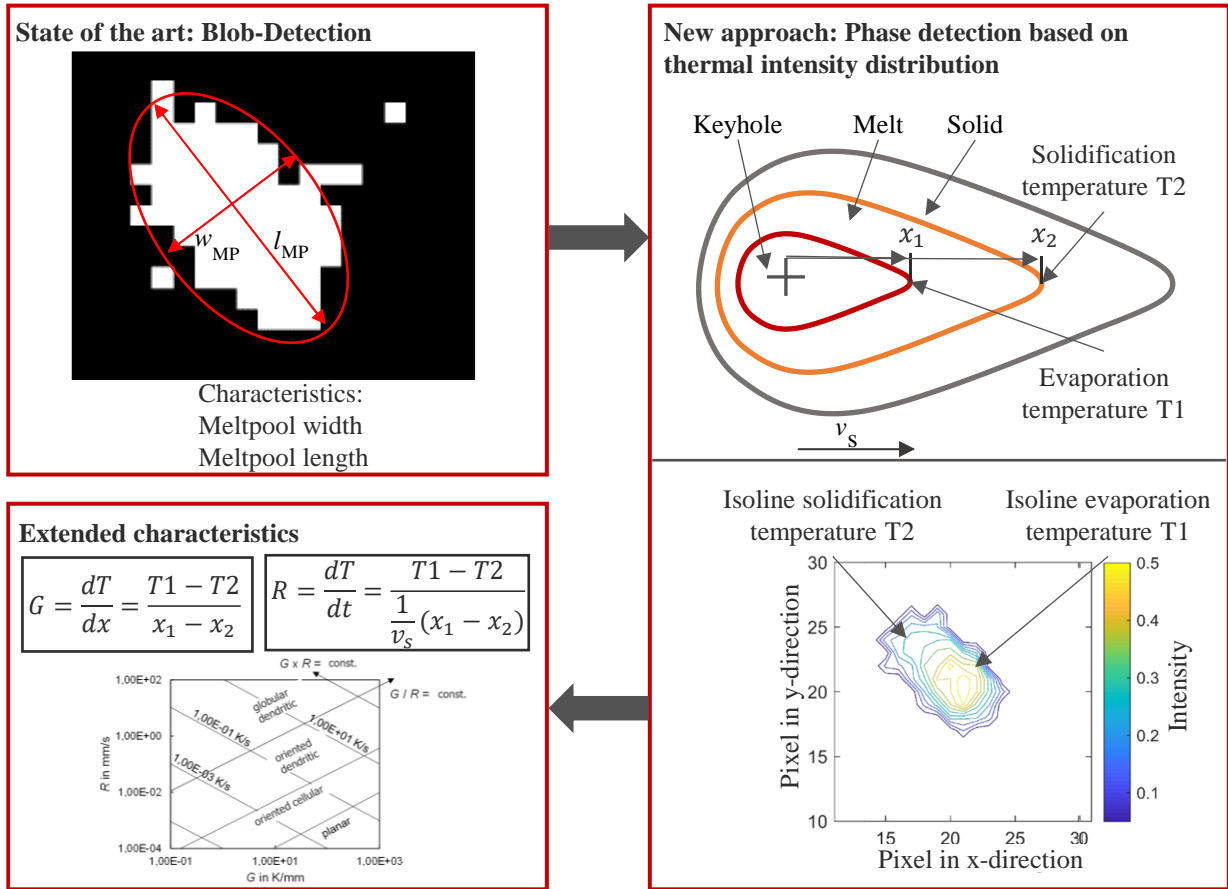


Figure 2: Schematic concept of the solidification evaluation

Focus of this work is the evaluation of the solidification process using a high speed camera (HSC). The HSC is implemented on an PBF-LB manufacturing system and the influence of the process on the thermal radiation intensity evaluated. By defining two referenced intensity values, characteristics for the solidification rate and temperature gradient can be derived (Figure 2). Based on single melt tracks the method is validated.

### Research methodology

A commercially available PBF-LB/M system M290 from EOS GmbH (Krailling, Germany) is used to conduct the experiments. This system uses a 400 W single-mode fibre laser with a wavelength of 1060 nm focused to a spot size of 100  $\mu\text{m}$ . The building volume has a size of 250 mm x 250 mm x 325 mm. Gas atomized stainless steel 316L powder is used for all experiments in this study. A scanning electron microscope (SEM) analysis of the powder is used to determine the particle distribution. Particles ranging from 11 to 54  $\mu\text{m}$  and a  $d_{50}$  of 25  $\mu\text{m}$  was determined. The PBF-LB/M system is extended by an on-axis high speed camera system plasmoEye (plasmo Industrietechnik, Austria) as shown in Figure 3. The camera has a pixel size of 14  $\mu\text{m}$  and a variable region of interest (ROI). The camera detects a wave length of 950 nm. The ROI is set to 80x40 pixel with a spatial resolution of 11.2 by 5.6 mm. The recording rate is set to 41,000 fps and an external trigger signal from the melt pool monitoring system is used to time stamp each image.

This time stamp is used to map each image with the position data from the melt pool monitoring system.

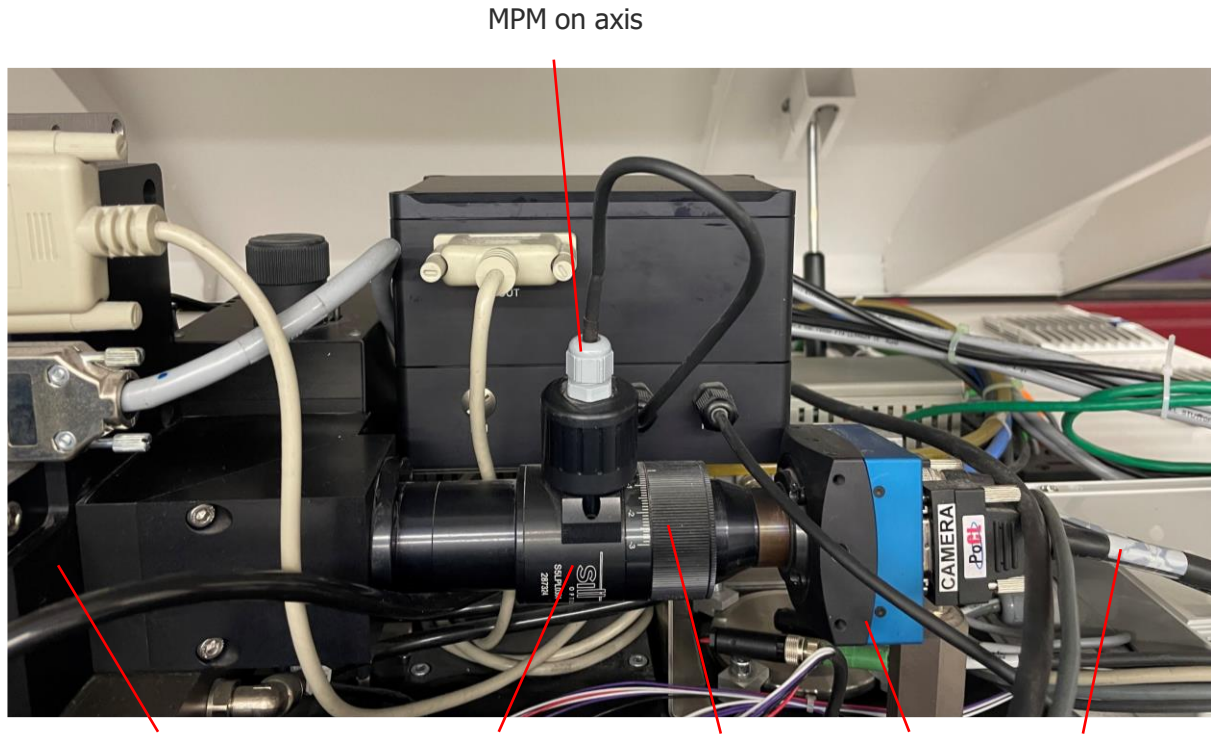


Figure 3: Experimental Setup - On-Axis High-Speed-Camera mounted on an EOS M290

The images are evaluated offline post process. Position- and exposure-dependent effects are taken into account by a correction and subsequent validation through a comparison of the generated melt track geometry with the evaluated melt track width. The temporally and spatially resolved intensity distribution as well as the weld mode and the melt pool depth represent the input variables for the modeling of the process-microstructure correlation. In addition, the temperature gradient is determined via the spatial distance between the solidification and sublimation iso-lines and the knowledge of the melting and boiling temperatures. The solidification rate is determined via the change in position of the solidification front over time. The investigations and data recording start with the production of one-dimensional single melt tracks and are continuously extended to two-dimensional melt track composites and three-dimensional layer composites. The influence of the build position, the scan vector direction, and the process parameters on the detection of the melt track via defined isolines of the melt pool intensity is examined. To evaluate the influence of these factors on the melt pool and the melt track detection, line tests are carried out and investigated by means of optical 3D measurement. The process parameters laser power and scan speed as well as the scan direction and the positioning in the build space are varied.

The detectability of the melt pool using the blob detection algorithm strongly depends on the HSC noise. To reduce noise and therefore improve the quality of the blob detection, a noise correction is developed. The mean value of each pixel is evaluated over 1,000 images from different build jobs and subsequently the difference between reference mean value and current

value derived for each image. The amount of 1,000 images is set to get a proper database and is also usable for other materials.

The basic algorithm for advanced evaluation is based on linking the melt pool geometry of the binary image with the intensity of the grayscale image (Figure 4). By overlaying the binary image with the intensity image, the noise is filtered out, as these would otherwise also be detected as meltpool. After superposition, the isolines can be formed for defined intensity values. This has the advantage that there is comparability across all experiments. The intensity level of the isolines can also be selected as a function of the exposure time in order to infer the intensity density, which enables a comparison of images taken at different exposure rates. The isolines show a significant correlation to the different phase states present and were determined using a best fit method. Orthogonal to the direction of the first major axis, measurement lines are then drawn at regular intervals along the length of the melt pool and the intersection points between the measurement line and the isoline are determined. The distance between the intersections on a measuring line is defined as the melt track width of the measuring point.

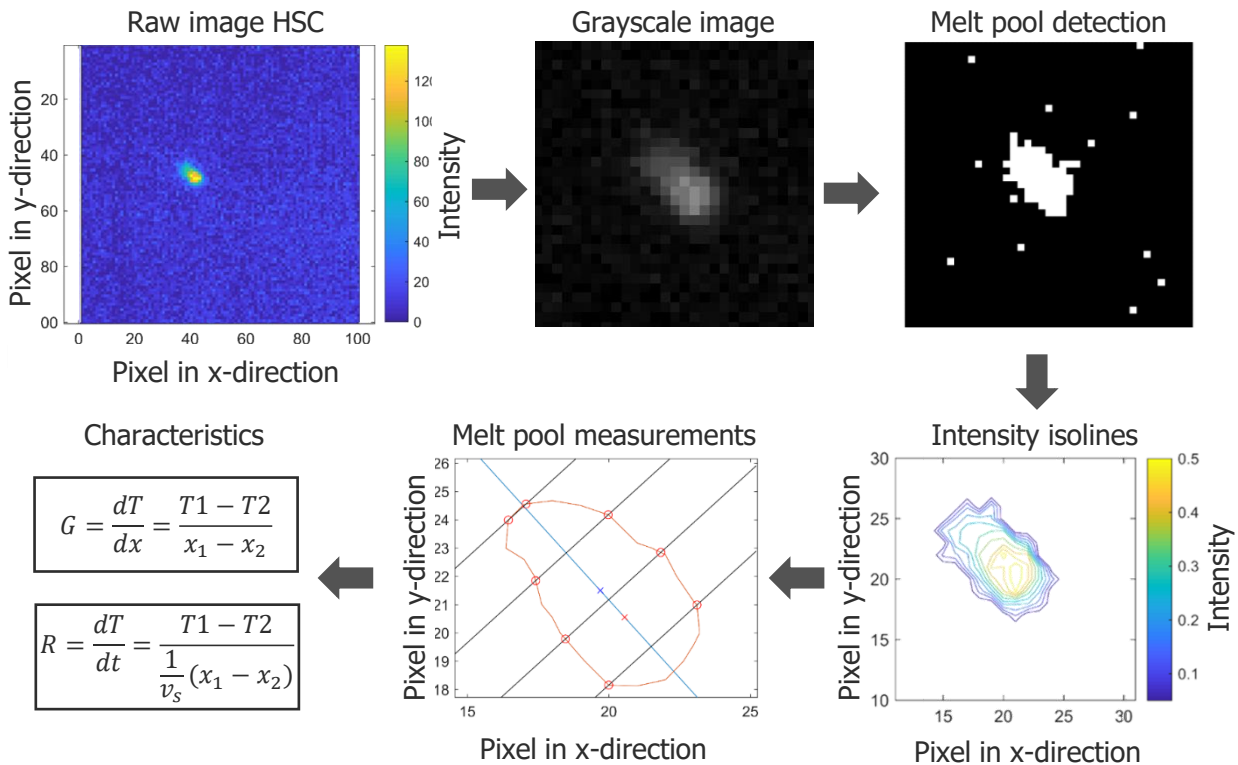


Figure 4: Schematic images of the central evaluation steps

The evaluation of the cooling rate via a comparative quantity from the HSC data is defined via the isoline of the keyhole edge (if a keyhole is present) and the solidification line (isoline of the intensity  $I = 0.2$  digits), which is of decisive relevance for the geometry. The temperature gradient corresponds to the difference between the melting temperature and the evaporation temperature and depends on the distance between the melting transition and the evaporation transition. For this purpose, a direction-dependent variable is defined. The cooling rate is defined by the time difference between the transition of the gaseous state at the keyhole edge to the melt and the solidification of the melt and is to be determined locally.

For the metrological calibration, three melt tracks are produced on a cuboid. The edge length of the cuboid is 10 mm. The distance between adjacent melt tracks is 3 mm, the distance to the edge of the cuboid is 2 mm. One side of the cuboid is parallel to each of the melt tracks.

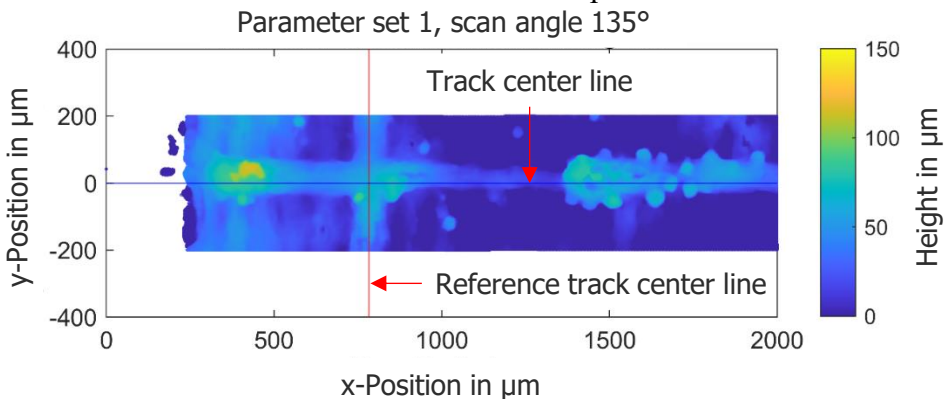


Figure 5: Example of the optical melt track measurement referenced by the intersection of the melt track and the reference track

For metrological referencing of the origin of the melt tracks, a reference melt track was manufactured perpendicular to the melt tracks at a distance of 0.5 mm from the edge of the cuboid (Figure 5). This thus crosses the melt tracks to be measured and can therefore be used as a starting point for measurement purposes in the height profile and by locating the process monitoring data. To evaluate the dependence of position and scan direction, eight cuboids per position were produced with varying scan directions at nine positions. The scan direction varies between  $0^\circ$  and  $315^\circ$  with an increment of  $45^\circ$ . The position varies evenly distributed in nine fields, three each in x-direction and three in y-direction. The basic influence of the process parameters on the detection and calibration of the isolines is done by varying the laser power and the scanning speed. The process parameter set qualified by the system manufacturer with a line energy of 0.18 J/mm is used as reference parameter set. A process parameter combination with reduced line energy of 0.09 J/mm in the range of heat conduction welding and a process parameter combination with increased line energy of 0.36 J/mm in the range of keyhole welding are selected.

## Results

The calculated mean noise of each pixel over 1,000 images of the HSC and subsequent consideration is used to decrease the noise by 85 % to 90 %. While isolines larger than the intensity of 0.4 digits can be interpreted as gaseous phase, isolines of intensities between 0.2 and 0.4 digits indicate melt. Isolines of intensities smaller than 0.2 digits indicate partially or completely solidified melt. Characteristic of the gaseous phase is the high fluctuation of the cross-sectional shape. An isoline stabilized in the cross-sectional shape near the keyhole indicates the transition between melt and keyhole. The transition between melt and solidified material can be seen by the transition into noise. From these isolines, further characteristic parameters are defined. These are the major axis lengths of the individual isolines as well as the width along the first major axis at defined measurement intervals. However, not all isolines are equally suitable for determining the melt pool width at defined measuring intervals. In particular, the isolines of intensity 0.1 to

0.2 digits exhibit a large dependence of the noise behavior and corresponding irregularities. Isolines from an intensity of 0.25 digits show a high stability in shape.

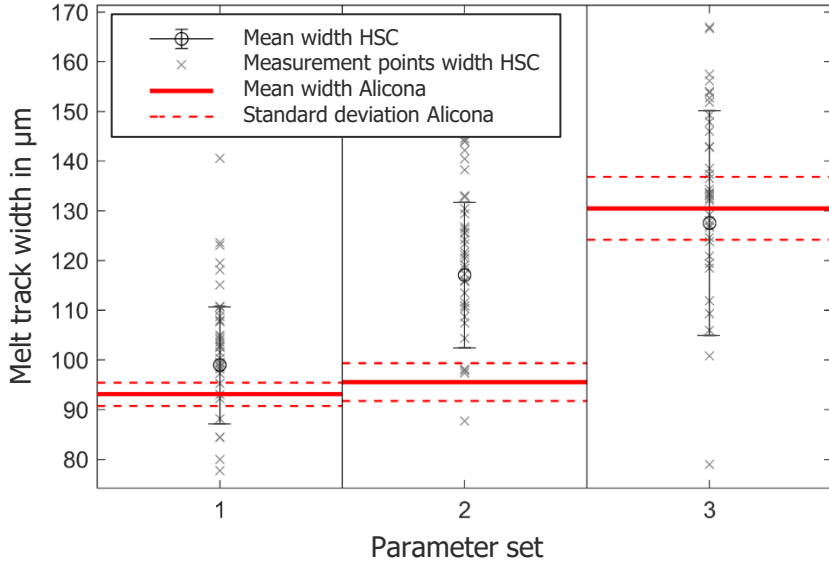


Figure 6: Comparison of melt track width for different parameter sets based on 3D-optical measurement (off-line, marked in red) and the high speed camera approach (marked in grey)

The detection of the melt track width via defined measuring points of the intensity isolines shows a dependence of the process parameters. The mean value of parameter set 3 (130 μm) is within the standard deviation of the melt track width determined by metrology measurement ( $130 \pm 7 \mu\text{m}$ ). The mean value of parameter sets 1 (98 μm) and 2 (117 μm) are outside the standard deviation (Parameter set 1:  $93 \pm 3 \mu\text{m}$ , parameter set 2:  $96 \pm 5 \mu\text{m}$ ) of the melt track width determined by measurement (Figure 6). Parameter set 2 shows the greatest deviation from the melt track width determined by measurement. The measuring points of parameter set 1 as well as the standard deviation overlap with the metrologically determined standard deviation. For all parameter sets, a large scattering of the measurement points can be seen.

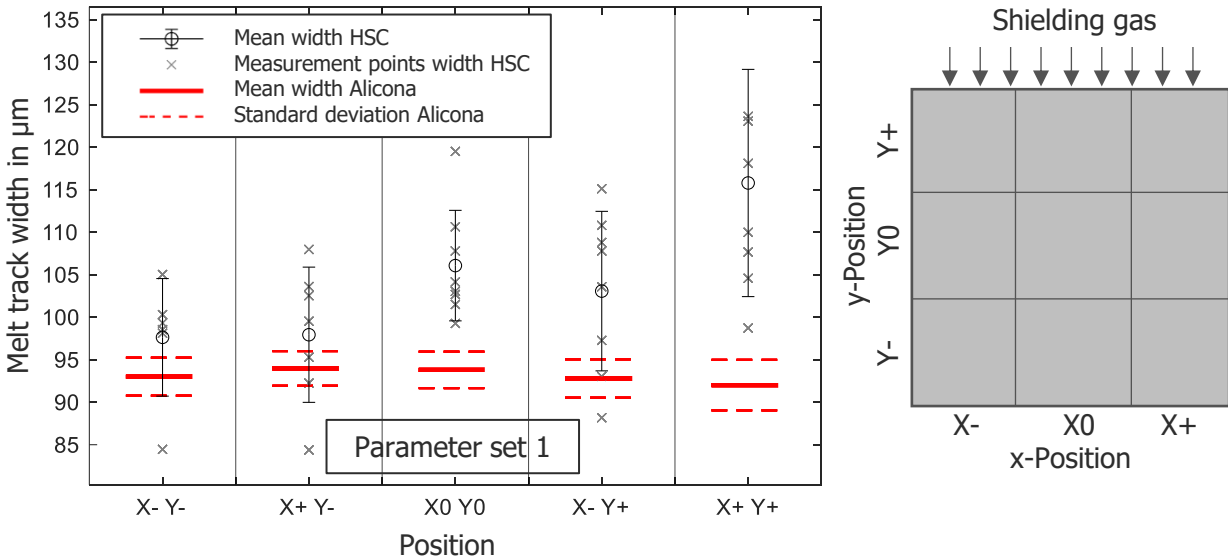


Figure 7: Comparison of melt track width for different positions based on 3D-optical measurement (off-line, marked in red) and the high speed camera approach (in-line, marked in grey)

The observation of the melt track detection via the isolines of the melt pool geometry shows a dependence on the position. The average melt track width is on average lower than the measured melt track width (Figure 7). Melt tracks which were produced on the X- position are detected as smaller by optical process monitoring compared to melt tracks which were produced on the X+ positions. A dependence on the y-position is not statistically significant.

The mean intensity shows high position dependency and varies between 0.03 and 0.07 digits. The X-Y- position shows the lowest mean intensity (0.03-0.04 digits). X-Y+ and X+ show the highest mean intensity (0.055-0.07 digits) as shown in Figure 8. The position-dependent intensity is used to adopt the characteristic intensity values for the evaluation. The characteristic intensity value for the transition from liquid to solid is set to 90% of the position depended mean intensity. The intensity value for the transition from liquid to gaseous is set to 90% of the position dependent maximum intensity.

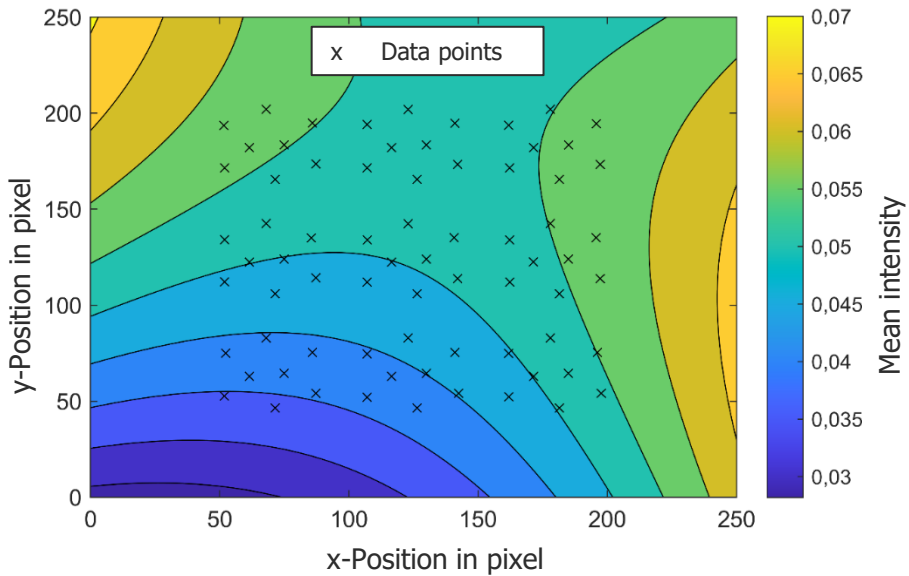


Figure 8: Influence of the position of the build platform on the detected mean intensity

A higher influence of the scan angle is seen when higher line energy density is used. The influence on the melt track evaluation is mainly for 90° (laser moves against shielding gas direction) and between 235° and 330° (laser is moving in shielding gas direction). The detected melt track via optical monitoring increases compared to other scan angles (Figure 9). The influence of the scan angle depends on the parameter set.

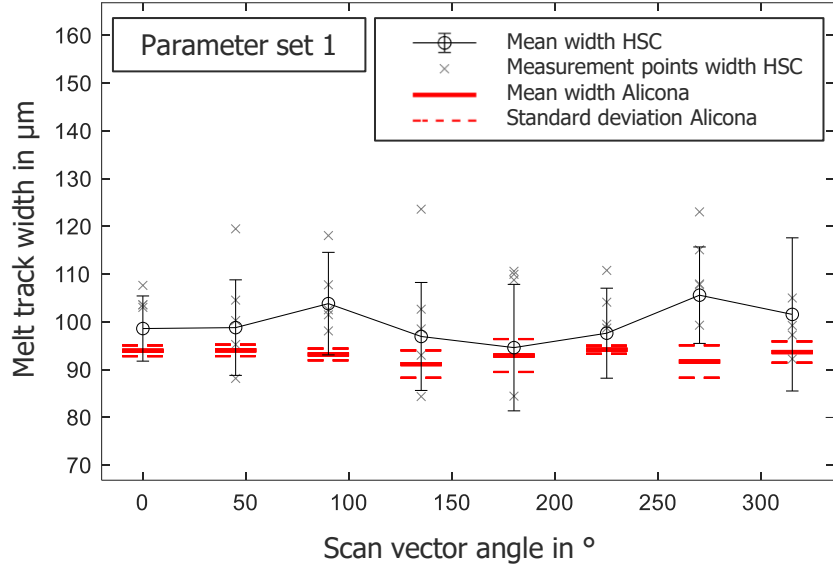


Figure 9: Comparison of melt track width for different scan angles based on 3D-optical measurement (off-line, marked in red) and the high speed camera approach (marked in grey)

Finally, the corrections based on position-dependency, scan vector angle, and noise were used to adopt the melt pool evaluation. This results in improved characteristics to characterize the melt pool and the resulting solidification. Deviations in the melt track are also detectable using the new approach (Figure 10).

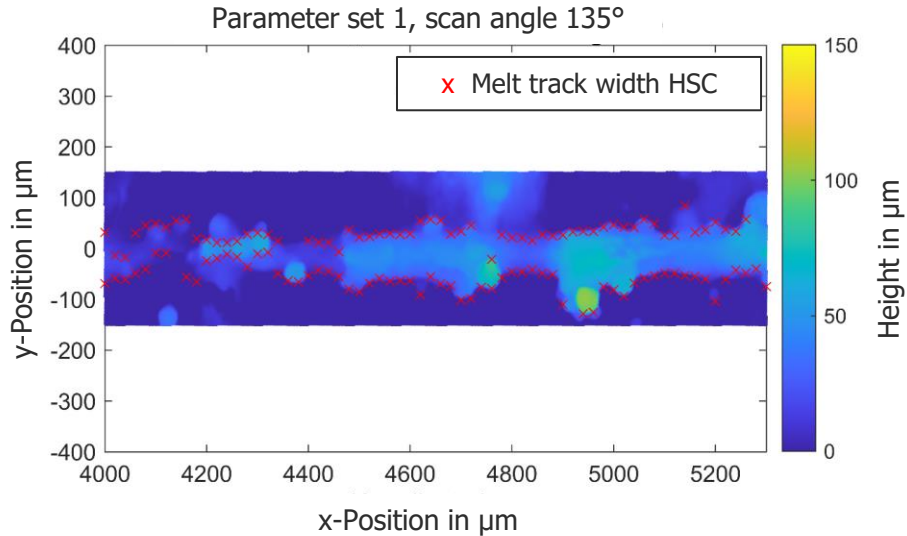


Figure 10: Illustration of the melt track width determination based on the HSC (red crosses) compared to the height profile of the melt track

Overall, the accuracy was improved, and the influence of position and scan angle was reduced (Figure 11). The deviation between melt track and evaluated melt pool characteristics was reduced to 1-5  $\mu\text{m}$ . There are two outliers ( $180^\circ$  and  $225^\circ$ ) using parameter set 1 with a deviation higher 5  $\mu\text{m}$ . However, the influence of the parameter set still exists. The evaluated melt pool

characteristics show higher results than the real melt track width. The deviation is between 4 to 20  $\mu\text{m}$ .

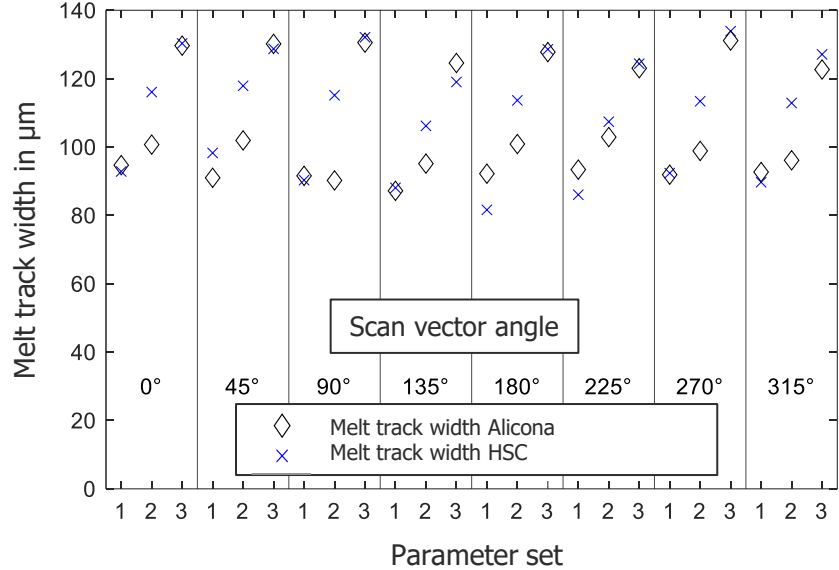


Figure 11: Final results of the melt track evaluation based on the HSC (blue crosses) compared to the optical determined melt track width for different parameter sets and scan angles

## Discussion

The detection of the melt pool geometry is based on the intensity distribution. The emission coefficient of the emitted thermal radiation of the melt pool depends on the material, temperature, and phase. Assuming homogeneous energy coupling, a uniform melt pool can be assumed to emit similar thermal radiation. The intensity of the detected thermal radiation would be constant under this assumption. This assumption neglects influencing factors of the energy coupling as well as changed detectability of the thermal radiation. The energy coupling is reduced by the angle of incidence of the laser beam and the scattering of the laser beam due to the formation of smoke above the vapor capillary and thus causes variable melt pool characteristics. In addition, the smoke causes scattering of the emitted heat radiation and thus influences the detectable intensity of the thermal radiation.

The effects investigated must be taken into account in the evaluation. For this, a separation of the effects must take place and a correction or adjustment of the evaluation algorithm must be made. Both the energy coupling and the heat radiation are position dependent. The consideration of the resulting fumes is dependent on both the scan angle of the laser beam and the process parameters. In the process, the stripe angle or the scan vector angle influences the interaction between the laser beam and the generated fume. If the laser travels in the opposite direction to the shielding gas direction, the fume generated in the interaction zone is transported out of the following interaction zone by the shielding gases. In the opposite case, when the scan vector direction and the shielding gas direction are identical, the fume is transported by the shielding gas into the new interaction zone and changes the laser beam properties geometry and power by scattering and reflection. Thus, deviating material properties can result from the changed laser-material interaction. The extent of the change depends on the combination of process parameters

and the inert gas flow. Furthermore, not only the laser radiation is changed, but also the detectable radiation in the process monitoring systems. Similar to the laser beam, the radiation emitted by the melt pool is modified by the fume. Scattering and reflection occur, with the result that the process radiation is less perceptible. All other alignments between the travel path of the laser beam and the shielding gas flow direction can be described by a partial scattering of the laser beam. The process parameters influence the quantity of the resulting fumes and thus the degree of scattering. High line energies tend to lead to greater fume generation due to vaporization of alloying elements. The scattering of the emitted heat radiation of the molten bath by flue gases is equally dependent on these same process phenomena.

The deviation of the melt track width for process parameter set 2 can be explained by the increased scanning speed. On the one hand, this results in a shorter exposure time and thus a longer melt pool length, and on the other hand, a higher scanning speed leads to faster removal from the area of welding fumes, which influence the laser radiation and the heat radiation. This prevents scattering of the laser radiation and the heat radiation by fumes.

### **Summary and outlook**

In this work a new approach to determine local thermal solidification characteristics is presented. A high speed camera with 41,000 fps is used to detect thermal radiation of the process zone in the wave length of 950 nm. The evaluation of the images is based on a melt pool detection and identification of intensity isolines, which define the characteristic transitions from gaseous to liquid and from liquid to solid phase. The experimental validation uses a best fit to compare metrological measurements with the derived melt track width from the HSC. The position, scan angle and process parameters are considered using correction factors within the evaluation. This results in good predicting quality of the melt track width with a low deviation less 5  $\mu\text{m}$  except for two outliers. To enhance the model quality and identify the limits of the method, more experimental investigations have to be made.

For further research the extension of the evaluation algorithm is focused to derive the thermal gradient. This concept has to be validated experimentally. Therefore, specimens have to be evaluated in terms of microstructural characteristics, e.g. by means of Electron-Backscatter-Microscopy. The current two-dimensional evaluation is supposed to include the melt track depth. Therefore, a model to predict the melt pool depth can be derived based on metallographic investigations or already established models. The ability to transfer to further materials has to be investigated. Based on the proposed approach, the experimental setup as well as the experimental design and the measurements can be copied to new systems and materials.

The overall aim of enabling data-driven processes is now provided with an approach to generate a high quality database. The sampling rate is able to match the process speed. The amount of information covers geometrical aspects and information which can be controlled by process adaptions. The developed approach provides local data of the solidification for ML-based process adaptions but also serves for part individual quality assurance tasks

## Acknowledgments

This research and development project is funded by the Federal Ministry for Economics and Climate Action (BMBK) within the “Technologietransfer-Programm Leichtbau” Program (funding number 03LB2009C) and implemented by the Project Management Agency Jülich (PTKA). The author is responsible for the content of this publication.

## References

- [1] DIN EN ISO/ASTM 52900:2022-03, Additive Fertigung - Grundlagen - Terminologie (ISO/ASTM 52900:2021); Deutsche Fassung EN\_ISO/ASTM 52900:2021, Beuth Verlag GmbH, Berlin.
- [2] R.C. Advincula, J.R.C. Dizon, Q. Chen, I. Niu, J. Chung, L. Kilpatrick, R. Newman, Additive manufacturing for COVID-19: Devices, materials, prospects, and challenges, *MRS Commun.* 10 (2020) 413–427. <https://doi.org/10.1557/mrc.2020.57>.
- [3] L. Schäfer, K. Skokov, J. Liu, F. Maccari, T. Braun, S. Riegg, I. Radulov, J. Gassmann, H. Merschroth, J. Harbig, M. Weigold, O. Gutfleisch, Design and Qualification of Pr–Fe–Cu–B Alloys for the Additive Manufacturing of Permanent Magnets, *Adv Funct Materials* 31 (2021) 2102148. <https://doi.org/10.1002/adfm.202102148>.
- [4] T. Wohlers, R.I. Campbell, O. Diegel, J. Kowen, N. Mostow, *Wohlers report 2021: 3D printing and additive manufacturing global state of the industry*, Wohlers Associates, Fort Collins, Colorado, 2021.
- [5] A. Großmann, J. Mölleney, T. Frölich, H. Merschroth, J. Felger, M. Weigold, A. Sielaff, C. Mittelstedt, Dimensionless process development for lattice structure design in laser powder bed fusion, *Materials & Design* 194 (2020) 108952. <https://doi.org/10.1016/j.matdes.2020.108952>.
- [6] H.M. Johannes Geis, Konstruktive Potentiale einer Mikrostrukturgradierung von topologieoptimierten L-PBF-Bauteilen, in: *DS 111: Proceedings of the 32nd Symposium Design for X*, The Design Society, 27 and 28 September 2021.
- [7] M. Grasso, A. Remani, A. Dickins, B.M. Colosimo, R.K. Leach, In-situ measurement and monitoring methods for metal powder bed fusion: an updated review, *Meas. Sci. Technol.* 32 (2021) 112001. <https://doi.org/10.1088/1361-6501/ac0b6b>.
- [8] H.-J. Bargel, G. Schulze, *Werkstoffkunde*, Springer Berlin Heidelberg, Berlin, Heidelberg, 2018.
- [9] G. Gottstein, *Materialwissenschaft und Werkstofftechnik*, Springer Berlin Heidelberg, Berlin, Heidelberg, 2014.
- [10] S.A. David, J.M. Vitek, Correlation between solidification parameters and weld microstructures, *International Materials Reviews* 34 (1989) 213–245. <https://doi.org/10.1179/imr.1989.34.1.213>.
- [11] A. Leicht, M. Rashidi, U. Klement, E. Hryha, Effect of process parameters on the microstructure, tensile strength and productivity of 316L parts produced by laser powder bed fusion, *Materials Characterization* 159 (2020) 110016. <https://doi.org/10.1016/j.matchar.2019.110016>.
- [12] J. Harbig, D.L. Wenzler, S. Baehr, M.K. Kick, H. Merschroth, A. Wimmer, M. Weigold, M.F. Zaeh, Methodology to Determine Melt Pool Anomalies in Powder Bed Fusion of Metals Using a Laser Beam by Means of Process Monitoring and Sensor Data Fusion, *Materials (Basel)* 15 (2022). <https://doi.org/10.3390/ma15031265>.

- [13] H. Merschroth, J. Harbig, M. Weigold, Defect detection based on sensor data fusion of optical monitoring systems in laser based Powder Bed Fusion, in: Laser Congress 2020 (ASSL, LAC), Washington, D.C, OSA, Washington, D.C., LTh1B.3.
- [14] J.-B. Forien, N.P. Calta, P.J. DePond, G.M. Guss, T.T. Roehling, M.J. Matthews, Detecting keyhole pore defects and monitoring process signatures during laser powder bed fusion: A correlation between in situ pyrometry and ex situ X-ray radiography, Additive Manufacturing 35 (2020) 101336. <https://doi.org/10.1016/j.addma.2020.101336>.
- [15] B.A. Fisher, B. Lane, H. Yeung, J. Beuth, Toward determining melt pool quality metrics via coaxial monitoring in laser powder bed fusion, Manuf. Lett. 15 (2018) 119–121. <https://doi.org/10.1016/j.mfglet.2018.02.009>.
- [16] H. Merschroth, M. Weigold, M. Kniepkamp, Predicting and Controlling the Thermal Part History in Powder Bed Fusion Using Neural Networks, SSRN Journal 57 (2021) 133. <https://doi.org/10.2139/ssrn.3785851>.
- [17] M.E. Kniepkamp, Methode zur bauteilindividuellen Prozesssteuerung beim selektiven Laserschmelzen. Dissertation.